water

MDPI

Article

Computational Fluid Dynamics–Discrete Element Method Numerical Investigation of Binary Particle Mixing in Gas–Solid Fluidized Bed with Different Drag Models

Chen Han [1], Xiaoling Fu [1,*], Xiaolu Guo [1], Wei Lu [2], Shaoqing Zhang [3], Hui Wang [4] and Yang Yang [4,*]

[1] College of Energy and Control Engineering, Changji University, Changji 831100, China; hanchen0622@outlook.com (C.H.); breeze_wong@163.com (X.G.)
[2] Suzhou Water Conservancy Design and Research Co., Ltd., Suzhou 215011, China; 18362990861@163.com
[3] Nanjing Water Planning and Designing Institute Co., Ltd., Nanjing 210001, China; 18252008908@163.com
[4] College of Hydraulic Science and Engineering, Yangzhou University, Yangzhou 225009, China; wanghui199712@163.com
* Correspondence: fxl@sdu.edu.cn (X.F.); yang_yang@yzu.edu.cn (Y.Y.)

Abstract: The fluidized bed is a critical reactor in the energy and chemical industries, where the mixing and agglomeration behaviors of binary particles significantly influence both the efficiency of reaction processes and the uniformity of final products. However, the selection of appropriate drag force models remains a subject of debate due to the variability in particle properties and operating conditions. In this study, we investigated the fluidization behavior of binary mixtures composed of two different sizes of Geldart-D particles within a fluidized bed, evaluating nine distinct drag force models, including Wen and Yu; Schiller and Naumann; Ergun; Gidaspow, Bezburuah, and Ding; Huilin and Gidaspow; De Felice; Syamlal and O'Brien; and Hill, Koch, and Ladd. We focused on four key parameters: particle mixing degree, migration characteristics, temperature variation, and mean pressure drop. Simulation results revealed that the choice of drag model markedly affected mixing behavior, migration dynamics, and temperature distribution. Notably, the Ergun; Gidaspow, Bezburuah, and Ding; and Hill, Koch, and Ladd models exhibited superior particle mixing uniformity. While the drag model had a relatively minor impact on particle temperature changes, its selection became critical in simulations requiring high-temperature precision. Regarding pressure drop, the Huilin and Gidaspow and Gidaspow, Bezburuah, and Ding models demonstrated smaller and more stable pressure drop fluctuations. These findings offer valuable theoretical insights into gas–solid two-phase flow under binary particle mixing and provide practical guidance for the design and operation of fluidized bed reactors.

Keywords: fluidized bed; drag model; CFD-DEM; particle mixing; unsteady flow

check for updates

Citation: Han, C.; Fu, X.; Guo, X.; Lu, W.; Zhang, S.; Wang, H.; Yang, Y. Computational Fluid Dynamics–Discrete Element Method Numerical Investigation of Binary Particle Mixing in Gas–Solid Fluidized Bed with Different Drag Models. *Water* **2024**, *16*, 3210. https://doi.org/10.3390/w16223210

Academic Editor: Bommanna Krishnappan

Received: 2 September 2024
Revised: 6 November 2024
Accepted: 7 November 2024
Published: 8 November 2024

Copyright: © 2024 by the authors. Licensee MDPI, Basel, Switzerland. This article is an open access article distributed under the terms and conditions of the Creative Commons Attribution (CC BY) license (https://creativecommons.org/licenses/by/4.0/).

1. Introduction

Fluidized beds are extensively utilized in the energy and chemical industries. Gas–solid two-phase flows within fluidized beds—such as those involved in coal powder combustion, biomass gasification, pyrolysis, and desulfurization—entail the mixing of multi-component particles [1,2]. In coal combustion processes, the interaction between catalyst particles and coal particles is critical for optimizing fluidization behavior and enhancing the combustion efficiency of coal. This underscores the importance of a comprehensive understanding of the mixing and flow dynamics of multi-component particles in fluidized bed systems [3].

Drag force is one of the most important interactive forces in gas–solid two-phase flow systems, significantly affecting the fluid dynamic behavior and the heat and mass transfer efficiency of particles. Most drag force calculations are based on empirical formulas that depend on the drag coefficient and the relative Reynolds number of the particles [4].

The calculation of drag force for individual particles is often relatively straightforward. The Schiller and Naumann (1933) drag model [5], well-documented in the literature, is primarily used for calculating drag in dilute gas–solid two-phase flow systems. This model is suitable for cases where the relative Reynolds number of the particles is less than 800, with a maximum deviation of 5% between the model's predictions and experimental results. To extend the application of drag models to higher particle Reynolds numbers, the DallaValle drag law revises the Schiller and Naumann (1933) drag model, making it applicable for particle relative Reynolds numbers up to 3000 [6]. Given that the forces acting on particles in gas–solid two-phase flows can be one-dimensional, two-dimensional, or even three-dimensional, the Morsi and Alexander (1972) drag model assumes that the drag coefficient depends solely on the particle's relative Reynolds number [7]. It introduces three empirically derived constants to adjust the drag coefficient, making the model suitable for flow conditions with particle relative Reynolds numbers ranging from approximately one (the onset of transitional flow) to several hundreds, or even tens of thousands (turbulent flow). However, the aforementioned drag models are only applicable to spherical particles. The Haider and Levenspiel (1989) drag model developed a calculation formula for the drag coefficient based on experimental data [8]. For spherical particles, the relevant coefficients in the drag coefficient calculation formula are fixed, whereas for non-spherical particles, the coefficients depend on the particle's sphericity. The irregular shape of particles and the mixing of particles of different sizes significantly influence the gas-solid two-phase flow field. The Ganser (1993) drag model considers the effects of particle shape and distribution on the flow by introducing Stokes' shape factor and Newton's shape factor [9], expanding its applicability in multi-component systems. In biomass energy materials, where most particles are cylindrical and fibrous, the Marheineke and Wegener (2011) drag model introduces the normal and tangential drag components relative to the axis of the cylinder to simulate the flow of fibrous particles [10].

For dense gas–solid two-phase flows, the calculation of the drag coefficient is typically adjusted by incorporating the fluid volume fraction [11]. The Wen and Yu (1966) drag model is applicable when the fluid volume fraction is less than 0.2 [12]. For fluid volume fractions between 0.2 and 0.7, the Ergun (1952) drag model is more suitable, particularly in cases involving flows through evenly distributed holes [13]. To further broaden the applicability of drag models, the Gidaspow, Bezburuah, and Ding (1992) model integrates both the Wen and Yu (1966) and Ergun (1952) models, yielding a drag coefficient calculation that can be applied across a wide range of fluid volume fractions [14]. However, since the Gidaspow, Bezburuah, and Ding (1992) drag model exhibits discontinuity at a fluid volume fraction of 0.8, the Huilin and Gidaspow (2003) drag model introduces a blending function to smooth the transition of the drag coefficient [15]. The Di Felice (1994) drag model improves upon the traditional Wen and Yu and Ergun models by incorporating a particle volume fraction term in the drag coefficient calculation, making it more appropriate for high-concentration particle flows [16]. In scenarios involving high particle concentrations and large particle numbers in two-phase flows, the Parameterized Syamlal and O'Brien drag model offers notable advantages [17]. To fully account for particle aggregation and inter-particle interactions in simulations, the Hill and Koch (2001) drag model is recommended [18]. The Hill, Koch, and Ladd (2006) drag model, which builds on the Hill and Koch (2001) model, employs a blending function to ensure continuity across different Reynolds numbers and solid volume fractions [19].

Recent advancements in numerical simulation techniques have significantly enhanced their role as a critical tool for analyzing complex multiphase fluid dynamics, particularly in fluidized bed systems [20]. In the case of circulating fluidized bed boilers, which typically involve gas–solid two-phase flow, two common numerical simulation methods are used: the Euler–Euler method and the Euler–Lagrange method [21]. The Euler–Euler approach, often implemented as a two-fluid model, treats both the fluid and solid phases as continuous media, accounting for potential chemical reactions and mass transfer phenomena between the two phases. A key challenge in this method lies in handling the dynamics of the

particles, including interactions between particles, the gas, and the walls [22]. The model incorporates particle dynamics using empirical closure terms, enabling the solid phase to exhibit the physical properties of the gas phase. The Euler–Lagrange method, on the other hand, views the fluid as a continuous phase and the solid as a discrete phase, making it more suitable for solving bed systems where particle motion and chemical reactions are significant factors [23]. In 1993, Tsuji et al. conducted the first discrete element method (DEM) simulation study of solid flow behavior in fluidized beds, achieving successful results. This method tracks particle motion trajectories by considering interactions between gas, solids, and wall collisions. In subsequent years, the combination of computational fluid dynamics (CFD) and DEM has been employed to further investigate gas-solid phase flows [24].

In specific industrial applications, selecting the most appropriate drag model is crucial for studying the flow patterns of gas–solid two-phase flows [25–27]. A comprehensive analysis reveals that many scholars have primarily focused on fluidization velocity, particle size distribution, distributor plate geometry, particle sizes, and pulse liquid phase flow. However, there has been relatively little research on the characteristics of drag models under binary particle mixing conditions. Therefore, this study utilizes the CFD-DEM bidirectional coupling method to investigate the influence of different drag models on the internal binary particle mixing conditions in a fluidized bed.

2. Numerical Simulation Method

2.1. Numerical Simulation Method of Fluidized Bed

The gas–solid two-phase coupled CFD-DEM model represents the gas phase using a continuous approach and the solid phase via the discrete element method. This model accurately simulates particle motion and determines specific particle parameters at the microscopic level. Consequently, the CFD-DEM is employed to examine various drag force models by selecting a constant inlet gas velocity. This approach facilitates the investigation of the underlying behaviors of the gas–solid phases within a fluidized bed.

2.2. Mathematical Model of the Gas Phase

The motion control equation for the gas phase accounts for the interaction forces between the gas phase and the particles. A standard two-equation turbulence model is adopted to establish the Navier–Stokes (N-S) equations. Finally, the SIMPLE algorithm is employed to solve the phase transition and chemical reaction processes. Consequently, the continuity equation and momentum conservation equation are obtained as follows [28]:

$$\frac{\partial(\varepsilon_g \rho_g)}{\partial t} + \nabla \cdot (\varepsilon_g \rho_g \vec{u}_g) = 0 \tag{1}$$

$$\frac{\partial(\varepsilon_g \rho_g \vec{u}_g)}{\partial t} + \nabla \cdot (\varepsilon_g \rho_g \vec{u}_g \vec{u}_g) = \nabla \cdot \vec{\tau}_g - \nabla p + \vec{F}_{p \to g} + \varepsilon_g \rho_g \vec{g} \tag{2}$$

In the above formula, ε_g is the volume fraction of gas phase, ρ_g is the gas density, u_g is the gas phase velocity after controlling the volume average, $F_{p \to g}$ is the momentum exchange between gas phase and solid phase, and τ_g is the gas phase stress tensor. The expression is as follows:

$$\tau_g = \varepsilon_g \mu_g [\nabla \cdot \vec{u}_g + \nabla \cdot \vec{u}_g^{\,T}] + \varepsilon_g (\lambda_g - \frac{2}{3}\mu_g) \nabla \cdot \vec{u}_g \vec{I} \tag{3}$$

where I is the unit tensor and μ_g and λ_g are the shear and bulk viscosity of the gas phase, respectively.

2.3. Solid Phase Control Equation

For the solid phase, each particle is regarded as an independent computational object, and its position and other physical property-related information is preserved in the compu-

tation, which is implemented as follows: for a solid phase containing N spherical particles, which have the same diameter and density, the particles are described in the Lagrangian coordinate system at the moment, t, of the computation as:

$$\{X_i(t),\ u_i(t),\ \omega_i(t),\ D,\ \rho,\ i = l, \ldots,\ N\} \tag{4}$$

where $X_i(t)$ is the position of the i-th particle as shown and $u_i(t)$ and $\omega_i(t)$ denote linear and angular velocities, respectively. D Indicates particle diameter, ρ Indicates particle density and the i-th particle mass, m_i, and rotational moment of inertia, I_i, are $\rho\frac{\pi D^3}{6}$ and $\frac{m_i D^2}{10}$, respectively.

$$\frac{dX_i(t)}{dt} = u_i(t) \tag{5}$$

$$m_i\frac{du_i(t)}{dt} = m_i g + F_d^{(i\in k)}(t) + F_c^{(i)}(t) \tag{6}$$

$$I_i\frac{d\omega_i(t)}{dt} = T^{(i)}(t) \tag{7}$$

where g represents the gravity acceleration, $F_d^{(i\in k)}$ represents the flow field force of the particle, i, in the grid point, k, including the pressure and the viscous force, $F_c^{(i)}$, representing the applied force of the collision, and $T^{(i)}$ represents the sum moment of the particle, i.

3. Numerical Simulation Scheme

In this study, ANSYS Fluent 2022 R2 and Rocky 2022 R2 are employed to simulate the dynamic behavior of a fluidized bed, shown in Figure 1 [29]. A 3D fluidized bed model is established, comprising walls, an air inlet, and an outlet, with dimensions of 0.1 m in length, 0.02 m in width, and 0.5 m in height. The grid and boundary conditions are defined, transient simulation is enabled, gravity acceleration is set, and the k-epsilon model is selected to describe turbulence. The energy equations are also enabled, and the flow conditions for the inlet and outlet are specified. In Rocky software, physical settings such as gravity direction and the numerical softening factor are configured. The model from Fluent is imported, and thermal boundary conditions are applied to the walls. The material properties of particles are then defined, and particles of varying sizes are created. By configuring input options and solver parameters, the particles are distributed, and simulations are initiated. After the simulations, the results are analyzed, with the 3D view and histogram illustrating particle flotation, settling, and mixing in different regions. The trend in particle mass within specific regions is examined, and the variation in particle temperature over time is observed. Additionally, the fluid temperature distribution is visualized in 3D, and the pressure drop is calculated to assess fluid flow properties. This study successfully simulates the fluidized bed's dynamic behavior by coupling ANSYS Fluent 2022 R2 and Rocky 2022 R2 software, offering in-depth analysis and interpretation of the results, which provides a theoretical foundation and technical support for future engineering applications. The specific parameter settings are provided in Table 1.

Table 1. Simulates the specific parameter settings.

Parameters	Symbol	Value	Unit
Gravity Y-direction	g	0	m/s^2
Gravity Z-direction	g	−9.81	m/s^2
Numerical Softening Factor	μ	0.1	-
Particles Density	ρ	1500	kg/m^3
Particles Young's Modulus	E	1×10^7	N/m^2
Particles Thermal Conductivity	κ	1.4	W/m·k
Particles Specific Heat	c_p	800	J/kg.K
Smaller Size	d_p	0.003	m

Table 1. *Cont.*

Parameters	Symbol	Value	Unit
Bigger Size	d_p	0.005	m
Seed Coordinates	$x\ y\ z$	0, 0, 0.01	m
Box bounds Center Coordinates	$x\ y\ z$	0, 0, 0.025	m
Box bounds Dimensions	$L\ H\ W$	0.1, 0.1, 0.1	m
Particle Mass	m	0.06	kg
Particle Temperature	T	363	K
Files to keep	-	2	-
Slover time	t	5	s
Slover General	-	GPU	-
Velocity Magnitude	u_g	*2*	*m/s*
Turbulence Hydraulic Diameter	*DH*	*0.1*	*m*
Inlet Temperature	*T*	*293.15*	*K*
Outlet Temperature	*T*	*293.15*	*K*
Time Step Size	t_{CFD}	*0.001*	*s*

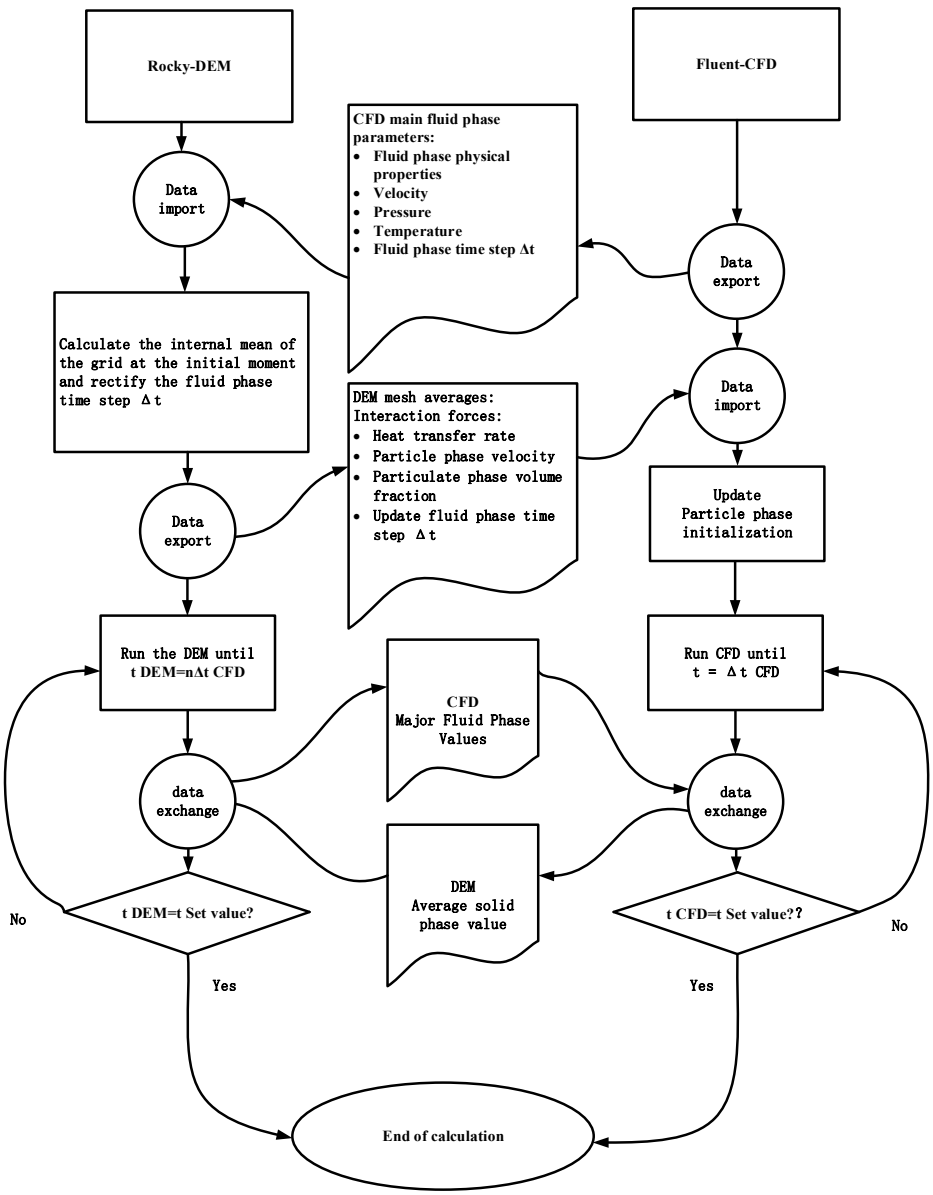

Figure 1. CFD-DEM numerical algorithm flow schematic [29].

4. Analysis and Discussion

Effect of the Drag Force Model on the Fluidization Characteristics

In a particle–fluid two-phase system, the drag force, which is influenced by factors such as the Reynolds number of the particles, their shape, and the temperature difference between the gas and particles, is the most significant force acting on the particles. Numerous drag force models have been documented for dense gas–solid two-phase flow, including the Wen and Yu model, Ergun model, Gidaspow, Bezburuah and Ding model, Huilin and Gidaspow model, De Felice model, Syamlal and O'Brien model, Hill, Koch, and Ladd model, and Hill and Koch model. To explore differences between dense gas–solid two-phase flow and single-particle drag model predictions, the Schiller and Naumann model for single-particle flow is added for comparative analysis. This study investigates the influence of different drag models on particle mixing by selecting a fluidized bed inlet flow velocity of 2 m/s and performing numerical simulations with nine drag models to analyze the particle evolution process, mixing dynamics, and temperature variations. As shown in Figure 2, the Schiller and Naumann model displays minimal particle flow evolution, while the Hill and Koch drag model exhibits limited particle mixing, behaving similarly to the Wen and Yu model in particle evolution but without distinct particle stratification. This is because the Hill and Koch model combines the Ergun and Wen and Yu models, automatically selecting the Wen and Yu model when local porosity exceeds 0.8. In contrast, the Hill, Koch, and Ladd model results in a higher bed height during particle evolution compared to other models, without significant stratification between large and small particles. This model extends the Hill and Koch model by describing the drag coefficient as a continuous function of the porosity field and relative Reynolds number, though the drag coefficient itself remains relatively constant. Comparisons of drag coefficients under the same Reynolds number and porosity reveal that the Hill, Koch, and Ladd model has a larger drag coefficient than other models. Further analysis of Figure 2 shows that the particle evolution processes of the Wen and Yu; Ergun; Gidaspow, Bezburuah and Ding; Huilin and Gidaspow; De Felice; and Syamlal and O'Brien models are similar, with the notable observation that larger particles gradually settle to the bottom of the bed over time, while smaller particles rise to the top.

To analyze particle mixing at different positions within the bed during flow, a partition labeling method is applied, dividing the particles into five distinct colors, labeled 0 through 5, from the bottom to the top of the fluidized bed. Figure 3 illustrates the mixing of large and small particles under various drag models, including the Wen and Yu; Ergun; Gidaspow, Bezburuah, and Ding; Huilin and Gidaspow; De Felice; Syamlal and O'Brien; and Hill, Koch, and Ladd models. Significant mixing occurs in the Hill and Koch drag model due to its large fluctuation amplitude, resulting in almost complete mixing across regions after 1 s and indicating a higher degree of mixing. In contrast, the Ergun; Gidaspow, Bezburuah, and Ding; Huilin and Gidaspow; and Syamlal and O'Brien models exhibit smaller fluctuation amplitudes, leading to more uniform particle mixing observed only after 4 to 5 s, particularly in the lower regions of the bed, where most particles remain as protodomain particles. The Wen and Yu, De Felice, and Hill and Koch drag models display minimal mixing between adjacent regions due to their lower fluctuation amplitudes, and after 5 s, most particles show little displacement, resulting in a low degree of mixing. The Schiller and Naumann drag force model, under these simulation conditions, shows almost no particle flotation, leading to an absence of significant particle mixing.

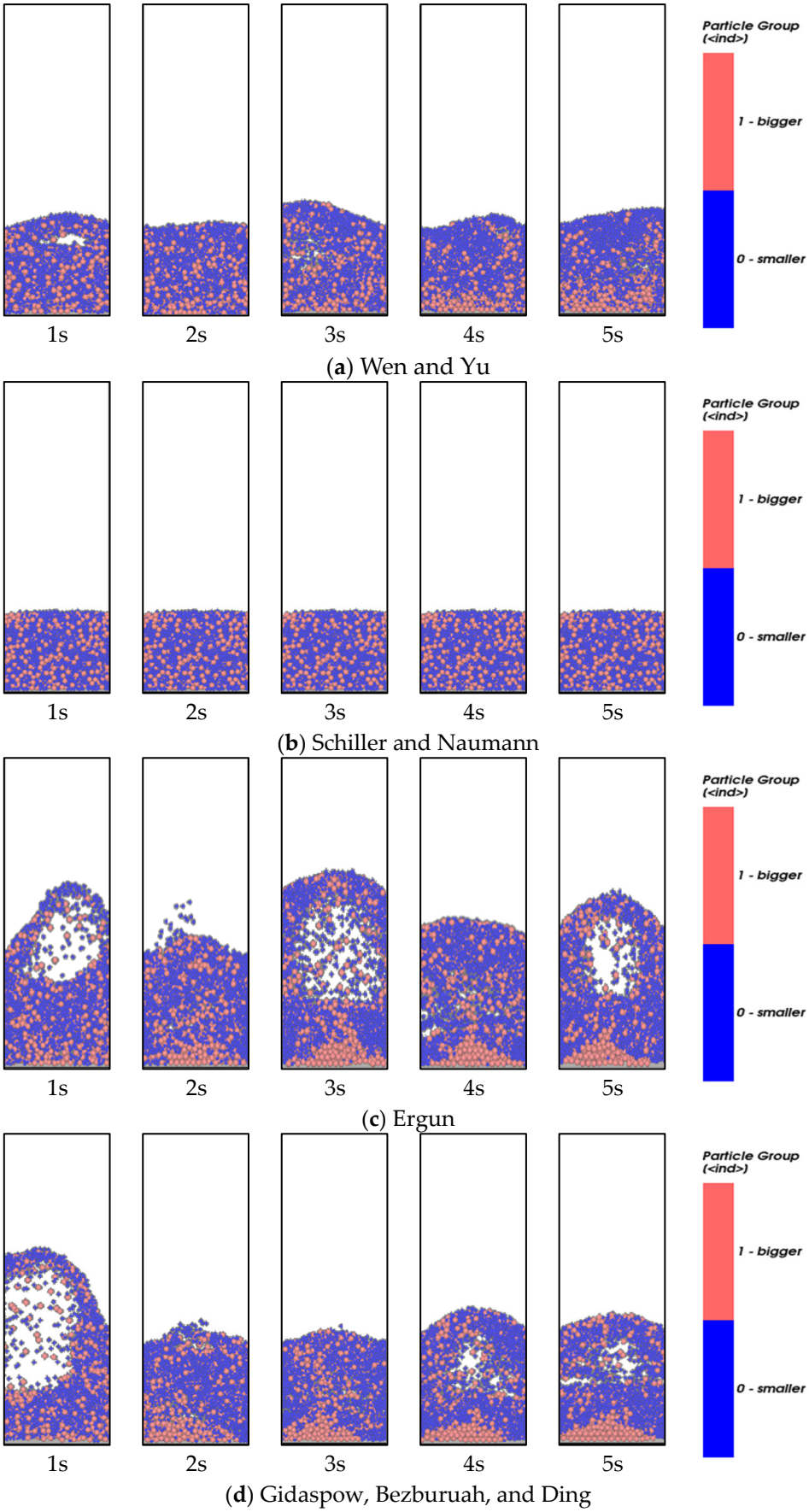

Figure 2. *Cont.*

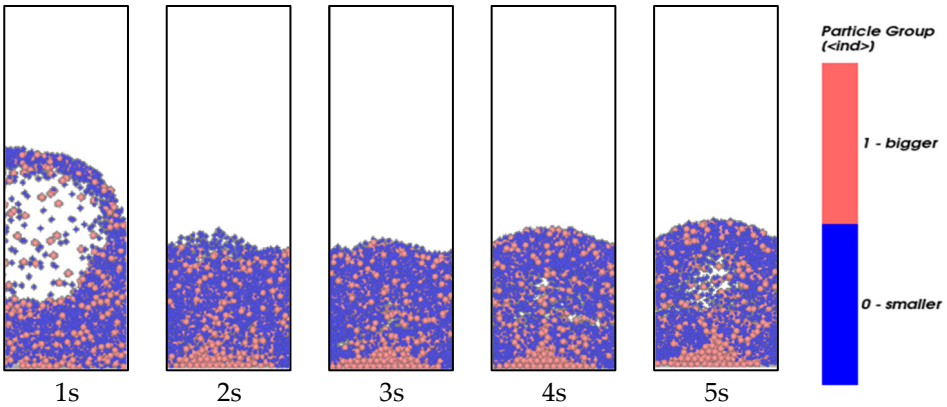

(**e**) Huilin and Gidaspow

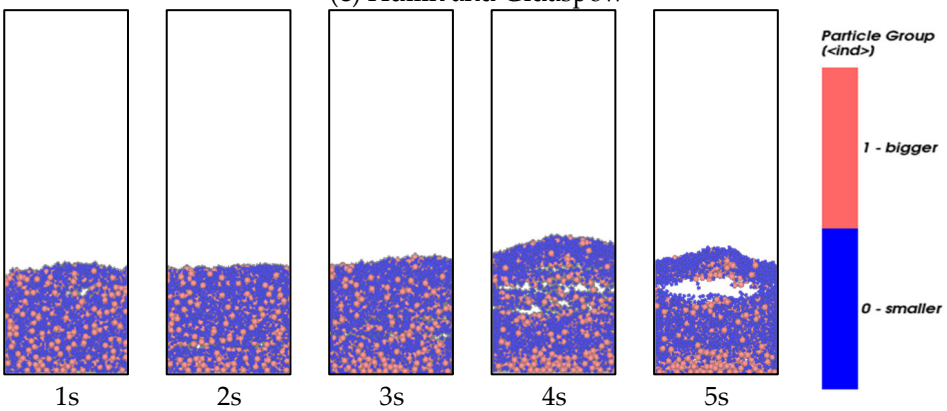

(**f**) De Felice

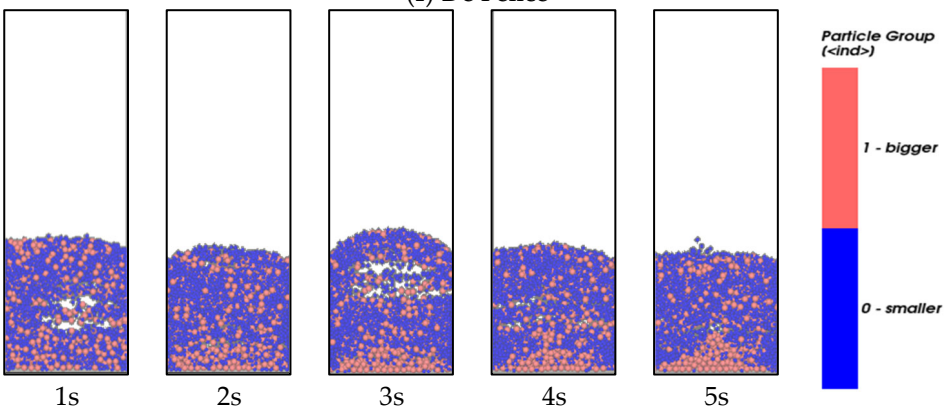

(**g**) Syamlal and O'Brien

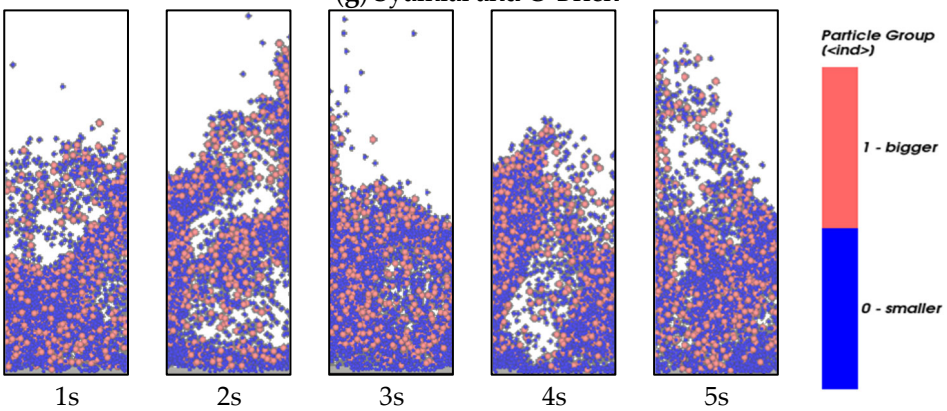

(**h**) Hill, Koch, and Ladd

Figure 2. *Cont.*

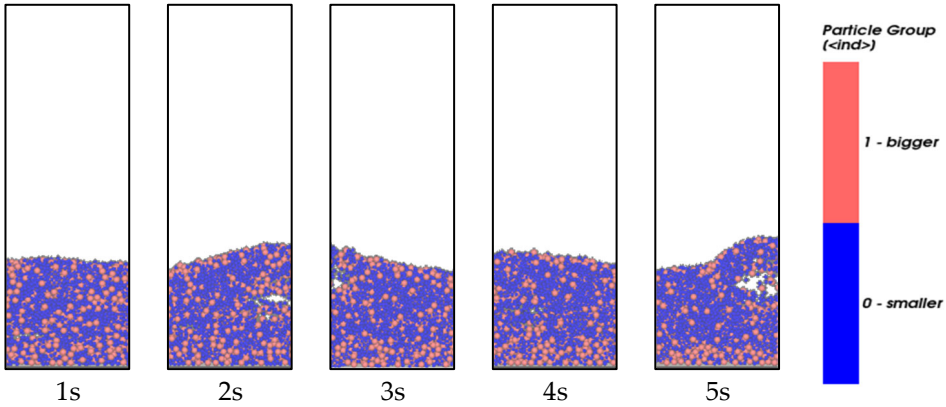

(**i**) Hill and Koch

Figure 2. Evolution of different drag models under mixing of large particles.

To focus the analysis on a specific part, a clustered bar graph is employed to examine particle mixing in different regions across various drag models during the simulation. As illustrated in Figure 4, the particles are divided into five distinct axis segments for this analysis. The first segment ranges from [1, 1.8], the second from [1.8, 2.6], the third from [2.6, 3.4], the fourth from [3.4, 4.2], and the fifth from [4.2, 5]. The fourth axis segment is selected as the specific region of interest. The simulation times of 1 s, 2 s, 3 s, 4 s, and 5 s are observed and discussed for each drag model, focusing on the ratio of particles within the fourth segment. The clusters of simulation times are then plotted according to the results.

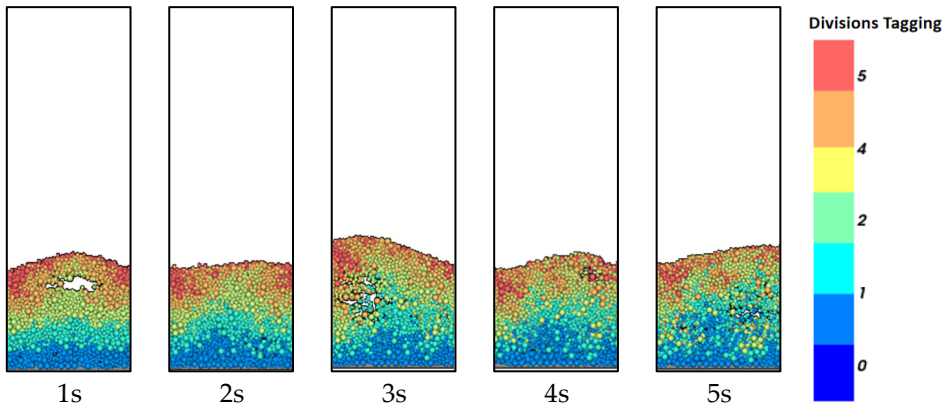

(**a**) Wen and Yu

Figure 3. *Cont.*

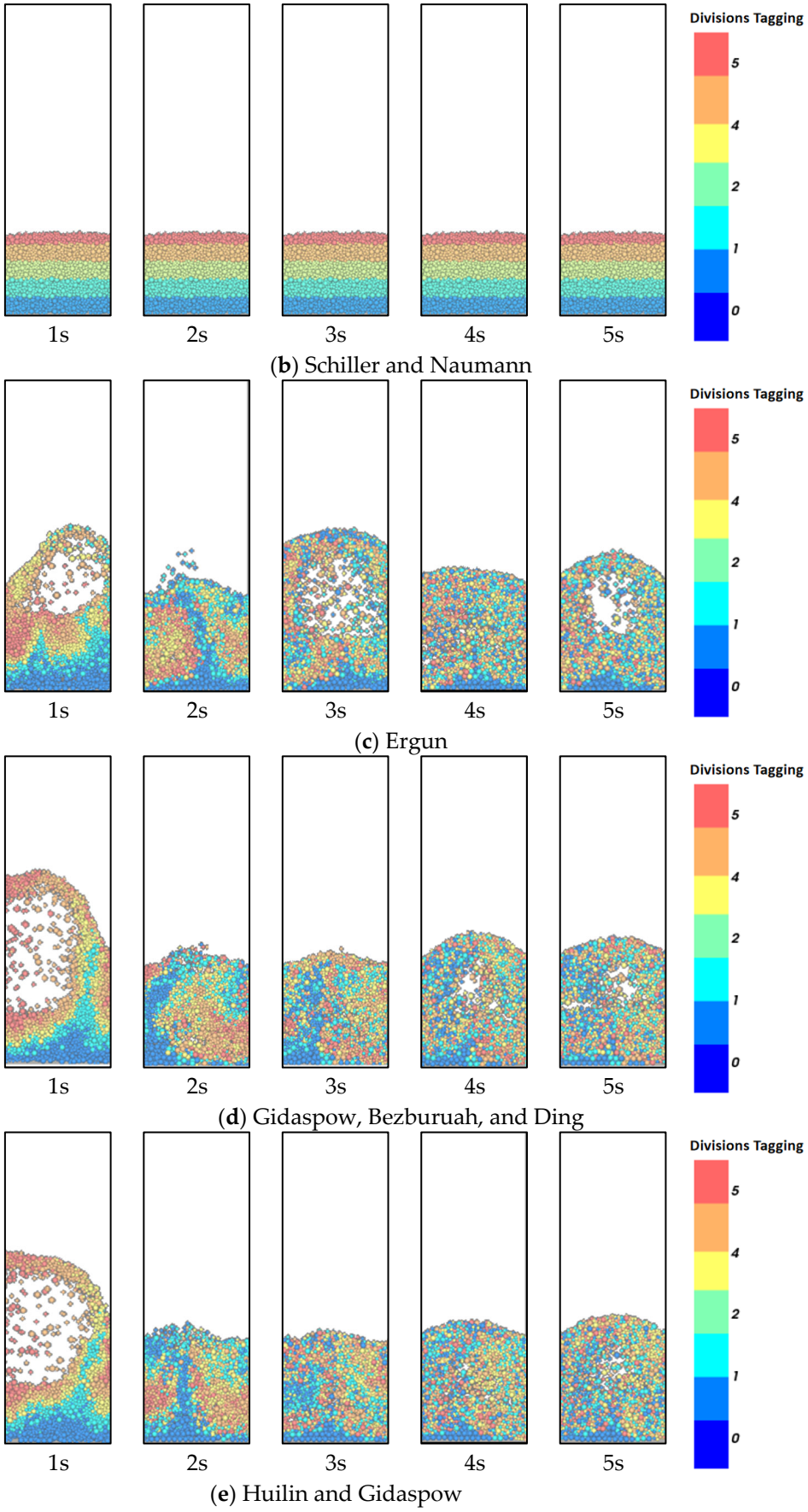

Figure 3. *Cont.*

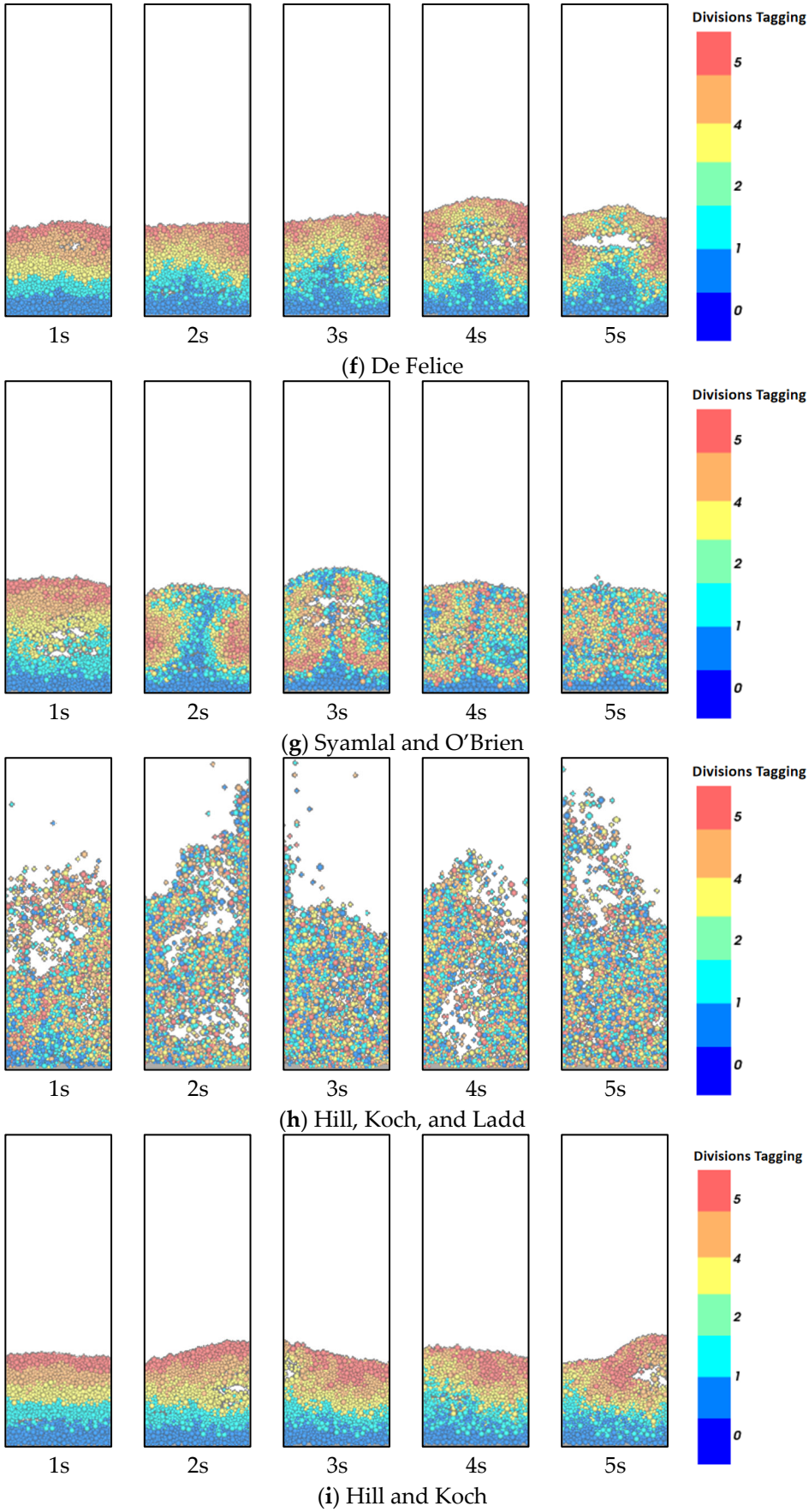

Figure 3. The hierarchical evolutionary mixing process of different drag force models under the mixing condition of large and small particles.

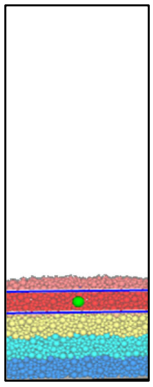

Figure 4. Schematic diagram of fluidized bed.

Figures 5–9 illustrate the particle mixing ratios in various drag models over time. The Schiller and Naumann drag model, serving as a reference, consistently maintains a 100% ratio because the particles do not float, resulting in no change in the defined region. In Figure 5, at 1 s, the Wen and Yu, Hill and Koch, and De Felice models show a high proportion of particles in the specific axis segment, indicating weak mixing, while the other drag models exhibit proportions around 40%. The Syamlal and O'Brien model, with a proportion of approximately 5%, displays significant fluidization characteristics at the initial moment. At 2 s (Figure 6), the proportion of all drag models in the specific axis segment falls below 60%, with the Wen and Yu, De Felice, and Hill and Koch models showing increased mixing compared to 1 s, while the remaining drag models show little change. In Figure 7, the Wen and Yu model experiences a notable decrease in mixing, with the proportion of particles in specific axial segments dropping from 50% at 2 s to 20% at 3 s, while the other models maintain similar particle mixing levels as at 2 s. By 4 s (Figure 8), the Wen and Yu and Hill and Koch models undergo significant changes, with the Wen and Yu model's particle proportion in specific axis segments increasing from 20% to 41%, indicating noticeable particle flow and a decline in bed height between 3 s and 4 s. Conversely, the Hill and Koch model continues to show a decreasing particle proportion in specific axis segments from 1 s to 5 s, reflecting weak remixing. The other drag models exhibit particle distributions similar to those at 3 s. In Figure 9, by 5 s, the mixing ratios across all drag models become relatively consistent, with the Ergun; Gidaspow, Bezburuah, and Ding; and Hill, Koch, and Ladd models achieving the most uniform mixing, as evidenced by relatively even particle distributions across the five regions.

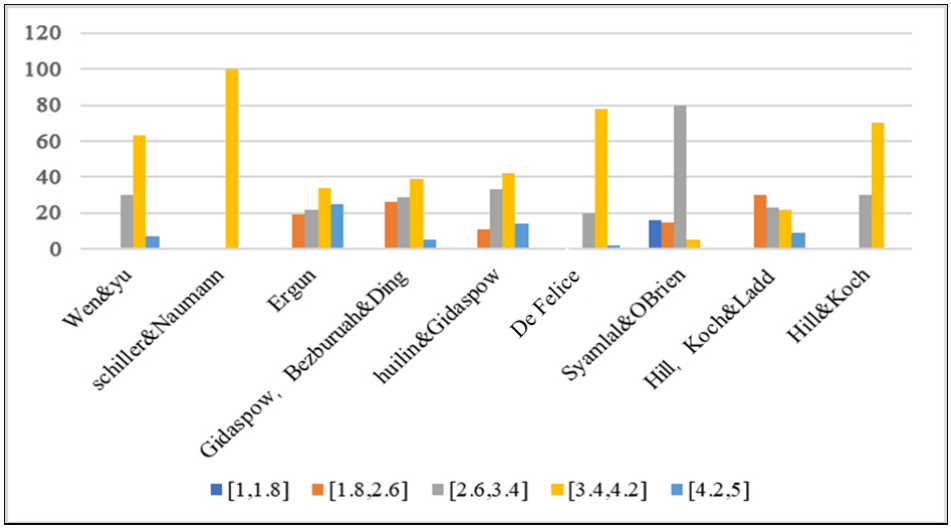

Figure 5. Particle mixing ratios for different drag force models at 1 s for specific axial segments.

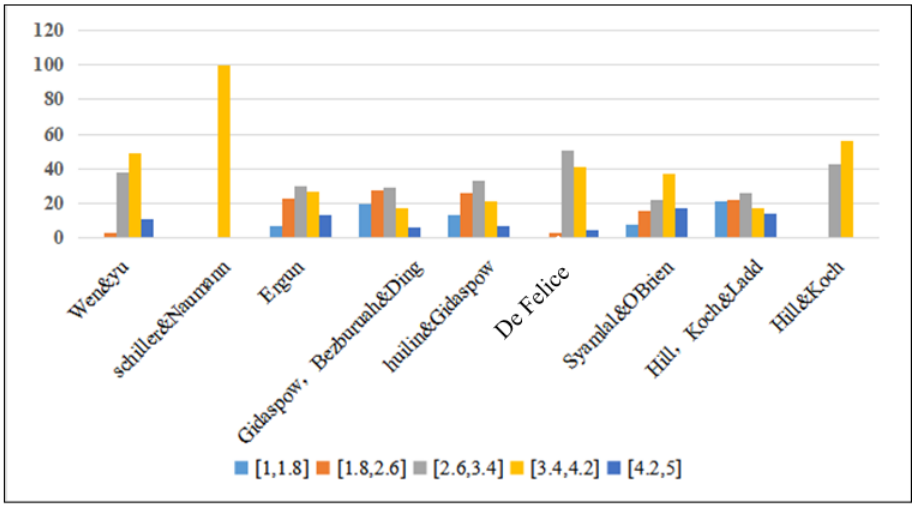

Figure 6. Particle mixing ratios for different drag force models at 2 s for specific axial segments.

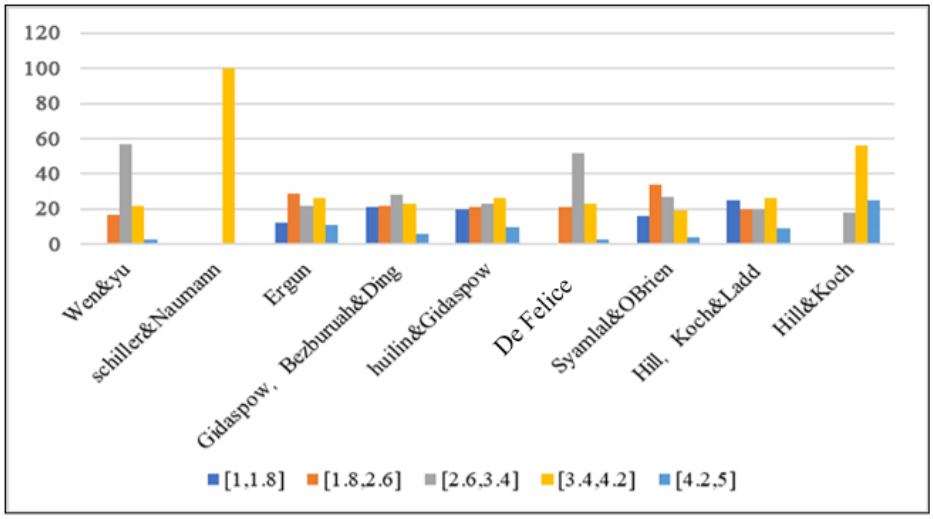

Figure 7. Particle mixing ratios for different drag force models at 3 s for specific axial segments.

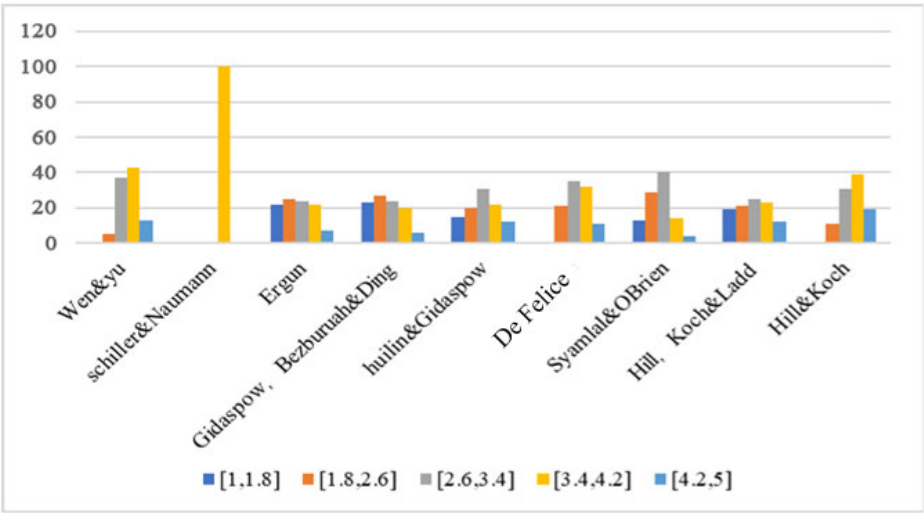

Figure 8. Particle mixing ratios for different drag force models at 4 s for specific axial segments.

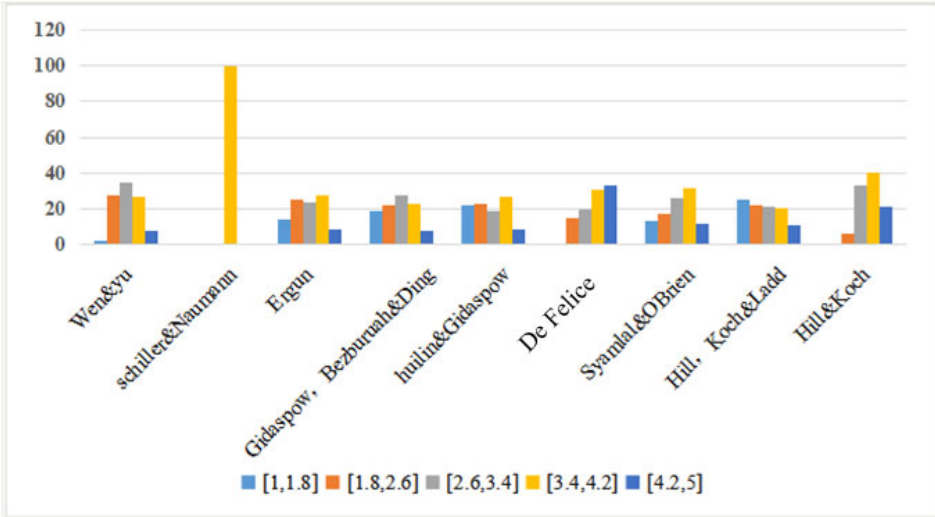

Figure 9. Particle mixing ratios for different drag force models at 5 s for specific axial segments.

To analyze the particle mass change during the flow process in a specific axis segment, the ratio of the particle mass in the defined region to the current particle mass is used as the initial reference for tracking the particle mass fraction fluctuation in the fourth axis segment for each drag model over time. As shown in Figure 10, the Hill, Koch, and Ladd drag model exhibits the least stable amplitude compared to other models, with the proportion of particles in the fourth axis segment remaining almost unchanged. In contrast, the De Felice, Syamlal and O'Brien, and Hill and Koch models show rapid frequency fluctuations with large amplitudes between 1 and 3 s, gradually stabilizing after 3 s. The Ergun, Gidaspow, Bezburuah and Ding, and Huilin and Gidaspow models display a steep drop in the 0 to 0.5 s range, followed by a gradual recovery and stabilization after 0.5 s, indicating that the fluidization processes of these models are relatively stable, with no significant agitation. The Schiller and Naumann drag model is used as a reference, as its particles exhibit minimal flotation, resulting in negligible changes in the defined region.

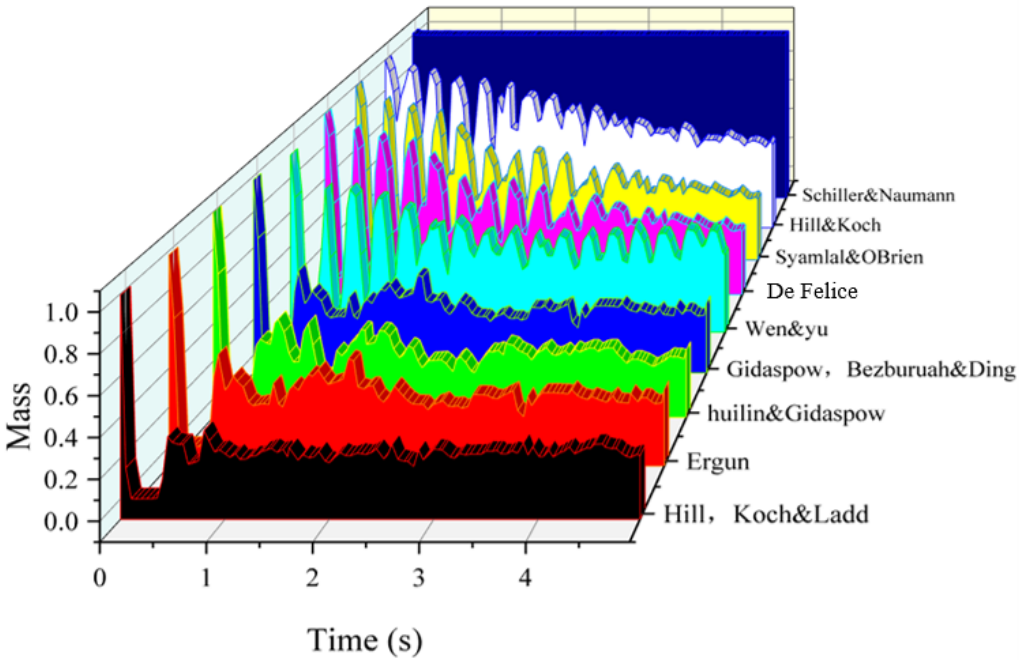

Figure 10. Initial labeled particle mass fraction fluctuation in the fourth axis segment of each drag model in 1–5 s.

Figures 11–13 provide insights into the particle temperature behavior across different drag models over time. Figure 11 shows that the Schiller and Naumann drag model experiences the least reduction in mean particle temperature, but due to the lack of particle flotation under the simulation conditions, it is not considered further. The final average temperatures of the other drag models are relatively close. In Figure 12, the lowest particle temperature over time indicates that the Hill, Koch, and Ladd model exhibits the smallest decrease in temperature during the 1 s to 5 s period, maintaining the highest minimum temperature, with a slight increase between 3 s and 4 s. The other drag models show a consistent, linear decrease in the lowest temperature. Figure 13 highlights the maximum temperature changes of particles from 1 s to 5 s, revealing three distinct trends: the Hill, Koch, and Ladd model shows the largest decrease in maximum temperature, while the Ergun; Gidaspow, Bezburuah, and Ding; Huilin and Gidaspow; and Syamlal and O'Brien models demonstrate a moderate decrease, with final temperatures being relatively close. The Wen and Yu, Schiller and Naumann, De Felice, and Hill and Koch models display the lowest maximum temperature curves but retain the highest final temperatures.

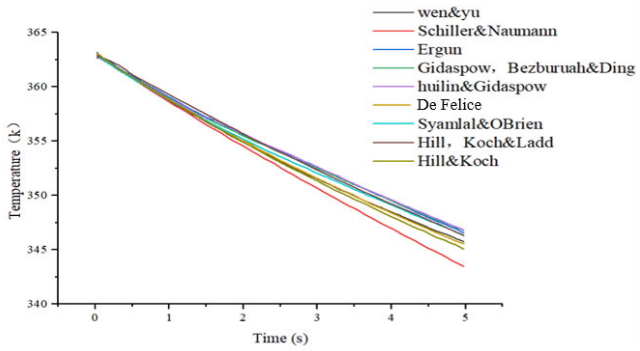

Figure 11. Average temperature change in 1 s–5 s particles in each drag model.

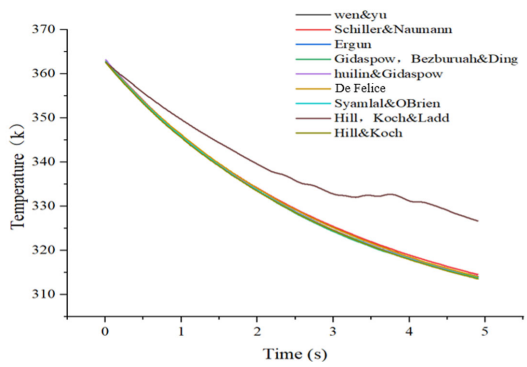

Figure 12. The lowest temperature change in 1 s–5 s particles in each drag model.

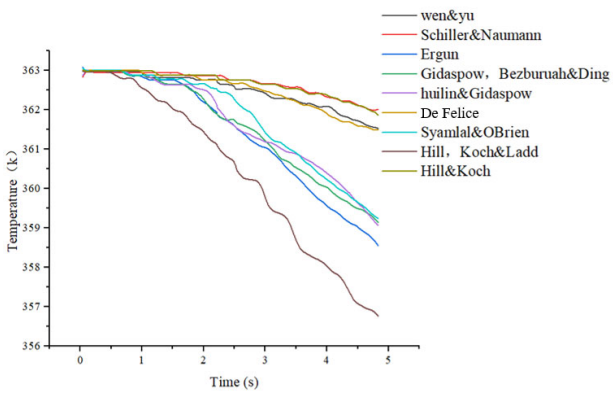

Figure 13. Change in the maximum temperature of 1 s–5 s particles in each drag model.

Figure 14 illustrates the temperature change process of both particles and fluid. The dotted area at the back of the fluidized bed particles represents the fluid temperature, as well as the temperature of all particles during the simulation. Between 0 s and 1 s, the temperature begins to decrease, as indicated by the blue color, which is caused by heat transfer between the particles and the fluid. The comparison of different drag models in the figure shows that drag influences particle fluidization behavior, thereby affecting the heat transfer between the particles and the fluid. It is important to note that during fluidization, when bubbles form, the fluid phase temperature is significantly higher in the center of the bubble.

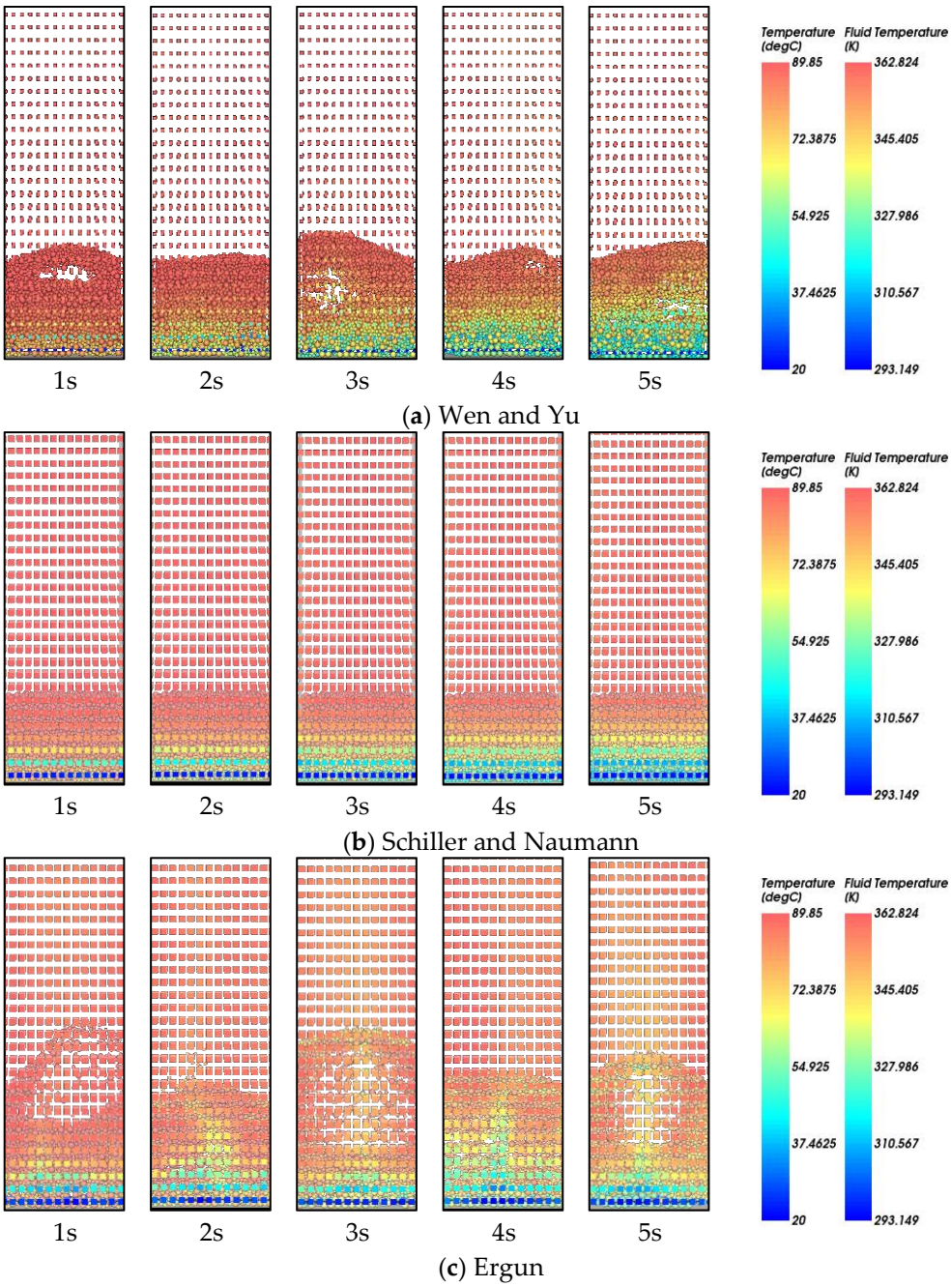

Figure 14. *Cont.*

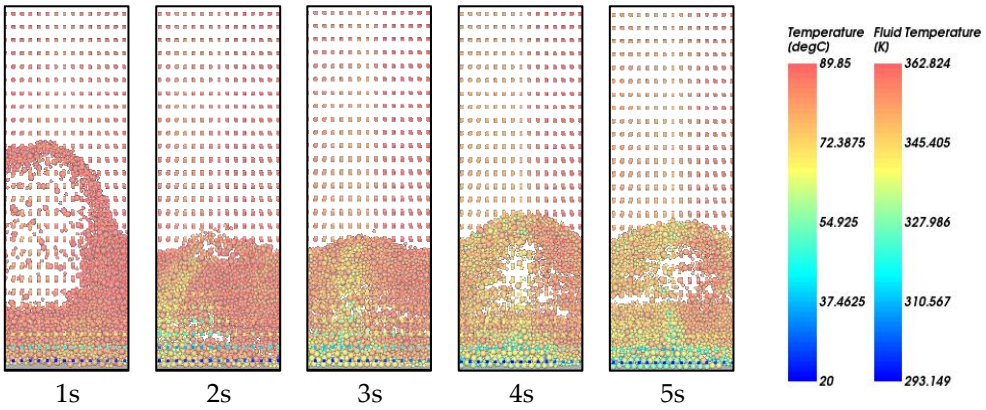

(**d**) Gidaspow, Bezburuah, and Ding

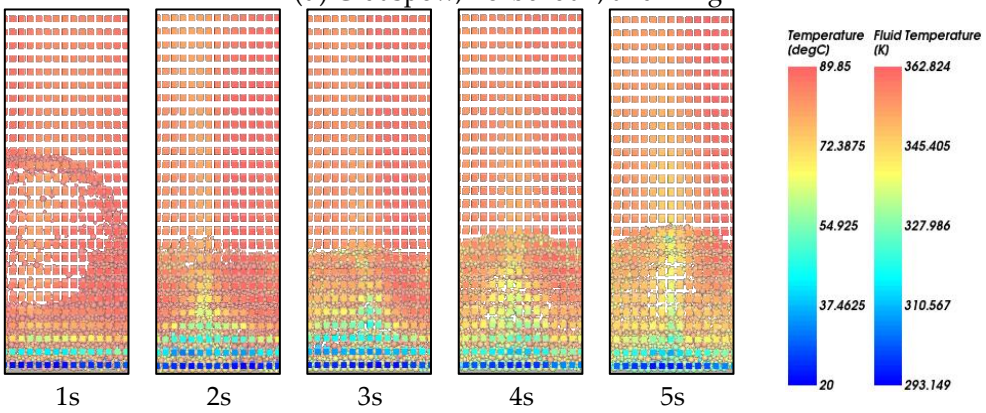

(**e**) Huilin and Gidaspow

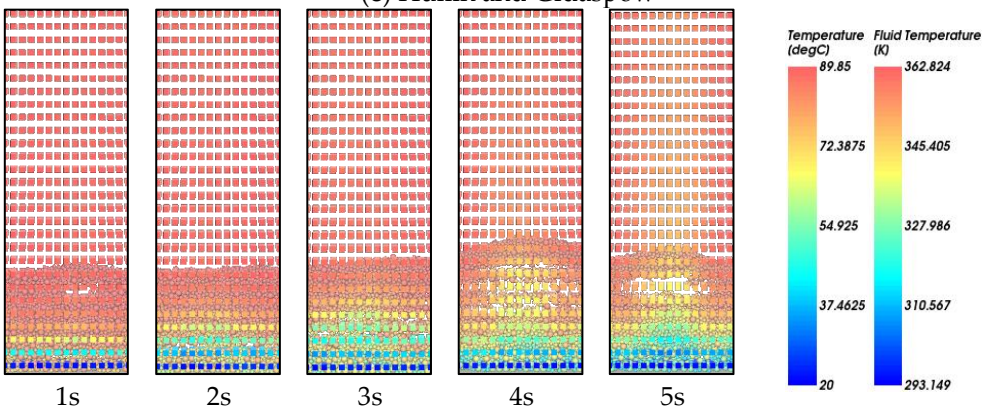

(**f**) De Felice

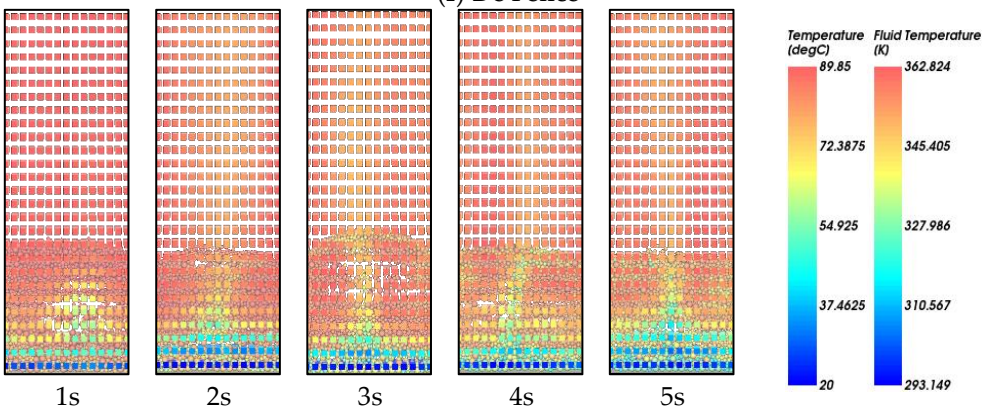

(**g**) Syamlal and O′ Brien

Figure 14. *Cont.*

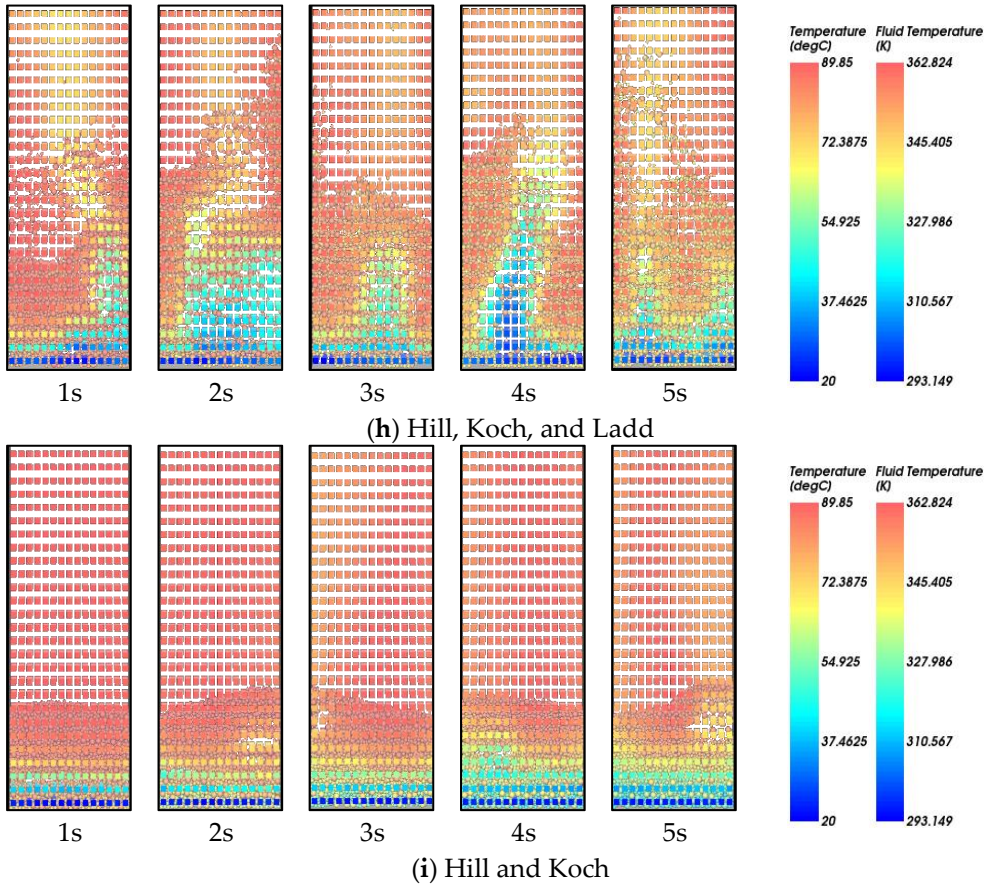

Figure 14. Change process of particle and fluid temperature.

Figure 15 shows the average pressure drop process in the fluidized bed. The Schiller and Naumann drag model serves as a reference, showing no oscillations in the pressure curve. In contrast, the Hill, Koch, and Ladd drag model exhibits the largest pressure fluctuation range with an unstable frequency. The pressure drop fluctuation ranges for the other drag models are relatively uniform, with the fluctuation frequencies of the Huilin and Gidaspow and Gidaspow, Bezburuah, and Ding drag models being notably consistent and stable.

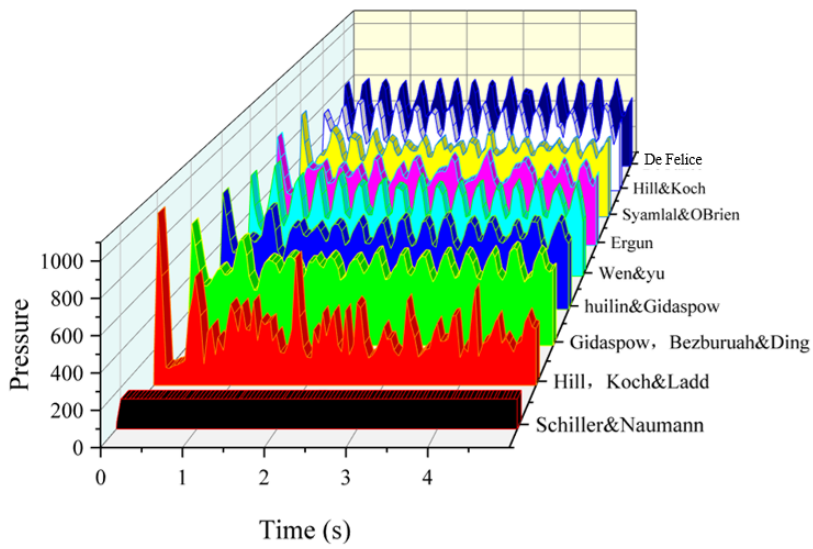

Figure 15. Pressure drop process of the fluidized bed.

5. Conclusions

This study employs the CFD-DEM to investigate the fluidization behavior of binary particle mixing in a fluidized bed under different drag models, aiming to analyze key parameters such as particle mixing degree, migration characteristics, temperature variation, and pressure drop. The research offers valuable insights into gas–solid two-phase flow under binary particle mixing conditions, providing a reference for future studies and practical applications in the design and optimization of fluidized beds. The conclusions drawn from the findings are as follows:

(1) Large particles generally settle to the bottom of the bed, while smaller particles float to the top. Among the drag models, the Huilin and Gidaspow model achieves particle stratification at 2 s, demonstrating its effectiveness in predicting particle movement trends.
(2) The Ergun; Gidaspow, Bezburuah, and Ding; and Hill, Koch, and Ladd models provide the most uniform particle mixing, with particle distribution in the five regions showing consistent mixing behavior. These models exhibit a strong capability for achieving uniform particle distribution across the bed.
(3) The choice of drag model has minimal impact on particle temperature at lower simulation temperatures. However, the Hill, Koch, and Ladd model shows a larger temperature variation range, making it more suitable for simulations where temperature fluctuations are significant.
(4) The analysis of pressure change at both ends of the fluidized bed reveals that the Huilin and Gidaspow and Gidaspow, Bezburuah, Ding models exhibit stable and small pressure fluctuation ranges, making them ideal for applications requiring consistent pressure behavior.

Author Contributions: Methodology, S.Z.; Software, C.H.; Validation, X.F.; Formal analysis, X.F. and H.W.; Resources, X.G.; Writing—original draft, Y.Y.; Writing—review & editing, C.H.; Visualization, X.G.; Supervision, Y.Y.; Project administration, W.L. All authors have read and agreed to the published version of the manuscript.

Funding: Sponsored by Natural Science Foundation of Xinjiang Uygur Autonomous Region (2022D01C462).

Data Availability Statement: Data is contained within the article.

Conflicts of Interest: Author Wei Lu was employed by the company Suzhou Water Conservancy Design and Research Co., Ltd. Author Shaoqing Zhang was employed by the company Nanjing Water Planning and Designing Institute Co., Ltd. The remaining authors declare that the research was conducted in the absence of any commercial or financial relationships that could be construed as a potential conflict of interest.

References

1. Pielsticker, S.; Gövert, B.; Kreitzberg, T.; Habermehl, M.; Hatzfeld, O.; Kneer, R. Simultaneous investigation into the yields of 22 pyrolysis gases from coal and biomass in a small-scale fluidized bed reactor. *Fuel* **2017**, *190*, 420–434. [CrossRef]
2. Kunii, D.; Levenspiel, O. *Fluidization Engineering*; Elsevier: Amsterdam, The Netherlands, 2013.
3. Wei, L.; Lu, Y. Numerical investigation of binary particle mixing in gas-solid fluidized bed with a bubble-based drag EMMS model. *Adv. Powder Technol.* **2020**, *31*, 1529–1542. [CrossRef]
4. Marchelli, F.; Hou, Q.; Bosio, B.; Arato, E.; Yu, A. Comparison of different drag models in CFD-DEM simulations of spouted beds. *Powder Technol.* **2020**, *360*, 1253–1270. [CrossRef]
5. Crowe, C.; Schwarzkopf, J.; Sommerfeld, M.; Tsuji, Y. *Multiphase Flows with Droplets and Particles*, 2nd ed.; Taylor & Francis: Abingdon, UK, 2011.
6. DallaValle, J.M. *Micromeritics: The Technology of Fine Particles*; Pitman Publishing Corporation: London, UK, 1948.
7. Morsi, S.A.J.; Alexander, A.J. An investigation of particle trajectories in two-phase flow systems. *J. Fluid Mech.* **1972**, *55*, 193–208. [CrossRef]
8. Haider, A.; Levenspiel, O. Drag coefficient and terminal velocity of spherical and nonspherical particles. *Powder Technol.* **1989**, *58*, 63–70. [CrossRef]

9. Ganser, G.H. A rational approach to drag prediction of spherical and nonspherical particles. *Powder Technol.* **1993**, *77*, 143–152. [CrossRef]
10. Marheineke, N.; Wegener, R. Modeling and application of a stochastic drag for fibers in turbulent flows. *Int. J. Multiph. Flow* **2011**, *37*, 136–148. [CrossRef]
11. Koralkar, N.V.; Bose, M. Performance of drag models for simulation of fluidized beds with Geldart D particles. *Adv. Powder Technol.* **2016**, *27*, 2377–2398. [CrossRef]
12. Wen, C.Y. Mechanics of fluidization. *Fluid Part. Technol. Chem. Eng. Progress. Symp. Ser.* **1966**, *62*, 100–111.
13. Ergun, S. Fluid flow through packed columns. *Chem. Eng. Prog.* **1952**, *48*, 89.
14. Gidaspow, D. *Multiphase Flow and Fluidization: Continuum and Kinetic Theory Descriptions*; Academic Press: Cambridge, MA, USA, 1994.
15. Huilin, L.; Gidaspow, D. Hydrodynamics of binary fluidization in a riser: CFD simulation using two granular temperatures. *Chem. Eng. Sci.* **2003**, *58*, 3777–3792. [CrossRef]
16. Di Felice, R. The voidage function for fluid-particle interaction systems. *Int. J. Multiph. Flow* **1994**, *20*, 153–159. [CrossRef]
17. Syamlal, M.; O'Brien, T.J. Computer simulation of bubbles in a fluidized bed. In *AIChE Symposium Series*; AIChE: New York, NY, USA, 1989; Volume 85, pp. 22–31.
18. Koch, D.L.; Hill, R.J. Inertial effects in suspension and porous-media flows. *Annu. Rev. Fluid Mech.* **2001**, *33*, 619–647. [CrossRef]
19. Benyahia, S.; Syamlal, M.; O'Brien, T.J. Extension of Hill–Koch–Ladd drag correlation over all ranges of Reynolds number and solids volume fraction. *Powder Technol.* **2006**, *162*, 166–174. [CrossRef]
20. Zhao, Z.; Zhou, L.; Bai, L.; Wang, B.; Agarwal, R. Recent advances and perspectives of CFD–DEM simulation in fluidized bed. *Arch. Comput. Methods Eng.* **2024**, *31*, 871–918. [CrossRef]
21. Li, C.; Eri, Q. Comparison between two Eulerian-Lagrangian methods: CFD-DEM and MPPIC on the biomass gasification in a fluidized bed. *Biomass Convers. Biorefinery* **2023**, *13*, 3819–3836. [CrossRef]
22. Kannan, J.; Sande, P.C. Reinterpretation of the Geldart A powder classification based on Eulerian–Eulerian CFD simulation. *Int. J. Chem. React. Eng.* **2023**, *21*, 129–141. [CrossRef]
23. Guo, M.; Yu, J.; Wang, S.; Luo, K.; Fan, J. Study of biomass gasification combined with CO_2 absorption in a dual fluidized bed (DFB) using the Eulerian-Lagrangian method. *Chem. Eng. J.* **2024**, *483*, 148723. [CrossRef]
24. Tsuji, Y.; Kawaguchi, T.; Tanaka, T. Discrete particle simulation of two-dimensional fluidized bed. *Powder Technol.* **1993**, *77*, 79–87. [CrossRef]
25. Cheng, N.S. Comparison of formulas for drag coefficient and settling velocity of spherical particles. *Powder Technol.* **2009**, *189*, 395–398. [CrossRef]
26. Mirek, P.; Ziaja, J. The influence of sampling point on solids suspension density applied in scaling of the hydrodynamics of a supercritical CFB boiler. *Chem. Process Eng.* **2011**, *32*, 391–399. [CrossRef]
27. Mirek, P. A simplified methodolgy for scaling hydrodynamic data from Lagisza 460 MWC supercritical CFB boiler. *Chem. Process Eng.* **2011**, *32*, 245–253.
28. Alobaid, F. A particle–grid method for Euler–Lagrange approach. *Powder Technol.* **2015**, *286*, 342–360. [CrossRef]
29. Rocky, E.S.S.S. Rocky DEM Technical Manual; 2018. Available online: https://pdfcoffee.com/dem-technical-manualpdf-pdf-free.html (accessed on 1 July 2024).

Disclaimer/Publisher's Note: The statements, opinions and data contained in all publications are solely those of the individual author(s) and contributor(s) and not of MDPI and/or the editor(s). MDPI and/or the editor(s) disclaim responsibility for any injury to people or property resulting from any ideas, methods, instructions or products referred to in the content.